## Optical spin readout of single rubidium atoms trapped in solid neon

David M. Lancaster, Ugne Dargyte, and Jonathan D. Weinstein \*

Department of Physics, University of Nevada, Reno NV 89557, USA

(Received 6 October 2023; accepted 9 February 2024; published 1 March 2024)

In this work, we optically resolve and detect individual rubidium atoms trapped in solid neon. Additionally, we optically pump the rubidium's spin state using polarized light and measure the spin state via laser-induced fluorescence. When combined with the previously demonstrated magnetic field sensing capabilities of matrix-isolated rubidium atoms, these results are very promising for nanoscale sensing and for performing nuclear magnetic resonance (NMR) spectroscopy of individual molecules cotrapped in the matrix.

DOI: 10.1103/PhysRevResearch.6.L012048

Quantum sensing with optically addressable solid-state spins is an active area of research [1], motivated by applications in nanoscale magnetic field sensing [2–4]. These ideas have been realized in a variety of systems, perhaps most notably with nitrogen-vacancy (NV) centers in diamond. NV's have demonstrated not only magnetic detection of single nuclear spins in the bulk—the naturally occurring <sup>13</sup>C in the diamond—but also imaging of those nuclear spins with angstrom-level resolution [5–8]. Because it is not known how to introduce arbitrary molecules into bulk diamond, molecular sensing with NV's requires attaching molecules to the diamond surface [4,9,10]. Unfortunately, diamond surfaces suffer from magnetic field noise [11–13].

We propose using single-atom sensors trapped in a noblegas matrix [14]. The molecules to be sensed and imaged could be cotrapped within the bulk, circumventing surface issues. We would expect to be able to implant essentially any molecule that can be introduced into the vapor phase; trapping of small biomolecules has been demonstrated [15–17].

In prior work with ensembles of rubidium atoms trapped in solid neon, it was shown that the rubidium atoms retained all the properties needed for quantum sensing of magnetic fields [18,19]. The ability to optically control the rubidium spin state was demonstrated, along with the ability to measure the spin state through circular dichroism. The spin coherence time was measured to be on the order of 0.1 s when employing dynamical decoupling protocols for sensing AC magnetic fields at frequencies of hundreds of kHz. This long coherence time is due to both the favorable properties of the trapped atom and the magnetically quiet environment of bulk neon. This provides sufficient sensitivity to measure the magnetic field of a single unpolarized nucleus cotrapped in the neon matrix: nuclear magnetic resonance (NMR) spectroscopy of <sup>21</sup>Ne nuclear spins has already been demonstrated with Rb ensembles [19].

Published by the American Physical Society under the terms of the Creative Commons Attribution 4.0 International license. Further distribution of this work must maintain attribution to the author(s) and the published article's title, journal citation, and DOI.

These properties are very promising for using a single Rb atom trapped in neon as a quantum sensor to perform NMR spectroscopy of single molecules cotrapped in the solid. The rubidium atoms would be implanted at low density—to allow for individual atoms to be resolved optically—and the target molecules would be implanted at high density, making it likely to find a molecule at a sufficiently close distance such that the precession of its nuclei can be measured by the rubidium. The detection and imaging of these nuclei can be accomplished by the same protocols already demonstrated with NV centers [5–8]. But the viability of this quantum sensing proposal hinges crucially on the ability to measure the state of single rubidium atoms in the solid matrix.

The detection of single atoms in noble-gas matrices by laser-induced fluorescence (without spin state readout) was previously demonstrated by the nEXO collaboration for barium atoms in solid xenon [20]. In this work, we demonstrate the ability to both detect single rubidium atoms trapped in solid neon and to measure their spin state via laser-induced fluorescence (LIF).

A schematic of our cryogenic apparatus is shown in Fig. 1. The copper coldfinger is in vacuum, surrounded by a radiation shield (not shown). Similar to prior work [21], the sample is grown by vapor deposition onto a sapphire substrate connected to the coldfinger. To improve light collection efficiency, we use a hemispherical sapphire substrate, which serves as a "solid immersion lens" for a widefield microscope [22,23]. As shown in Fig. 1, the sample is grown on the exposed flat side of the substrate.

To excite LIF, the sample is illuminated with laser light at 786 nm [18,19]. The optical absorption spectrum of Rb in neon—for a given trapping site—is homogenously broadened [19]. Consequently, we expect the single-atom absorption spectrum of the atoms observed here to be identical to that reported in Ref. [19] for atoms that absorb at 786 nm. Typical powers are  $\sim$ 3 mW, with beam waists of  $\sim$ 0.2 mm and peak intensities of  $\sim$ 5 W/cm². The beam waist is chosen to be larger than the motion of the coldfinger, which is  $\lesssim$ 0.1 mm.

LIF from the atoms is collimated by a large-numericalaperture molded aspheric lens mounted to the coldfinger, which serves as the infinity-corrected objective lens of the microscope. This optics arrangement serves to reduce the

<sup>\*</sup>weinstein@physics.unr.edu; https://www.weinsteinlab.org

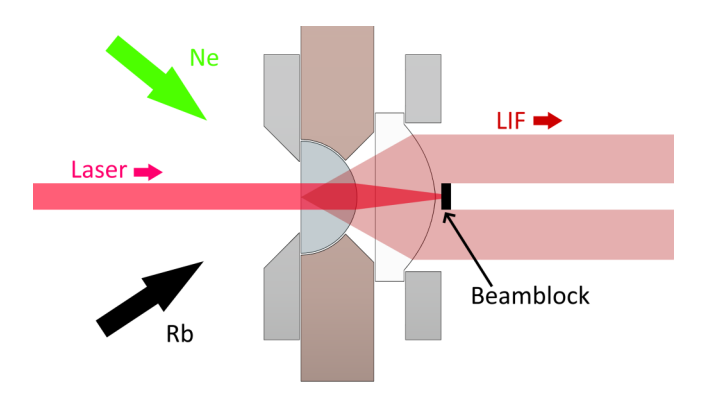


FIG. 1. Schematic of the copper coldfinger, as described in the text. A 10 mm diameter sapphire hemisphere is attached to the left side of the coldfinger and a commercial high-NA lens is attached to the right. A layer of indium connects each to the coldfinger, and an aluminum clamp holds each in place. The sample is grown on the flat surface of the hemisphere. The implanted atoms are excited by a laser beam from the left; the transmitted laser beam is blocked by a beam block at the right. (The size of both are exaggerated for visibility). The atomic LIF is collected and collimated by the lens, and sent to the right, out of the vacuum chamber.

blurring of the image from the motion of the coldfinger. A 2 mm wide strip behind the lens blocks the majority of the excitation light, while only blocking a small fraction of the LIF from the atoms. The LIF exits the cryostat through a series of windows. Outside the cryostat the LIF passes through a pair of color filters which significantly reduce the apparatusscattered light with only minor attenuation of the red-shifted atomic LIF [18]. After the filters, an achromatic doublet serves as the microscope's "tube lens" to form an image of the sample on a cooled sCMOS camera. We estimate the light collection efficiency to be  $\sim$ 18%, accounting for both the geometrical light collection and the transmission of the optical elements. As seen in Fig. 2, the LIF signal from a single atom in our cryostat has a FWHM of 3 µm. We believe the primary limit on the resolution of our imaging system is from chromatic aberrations, due to the broad LIF spectrum [18].

We were unable to measure the spectrum of the emitted LIF. Because the absorption spectrum is homogenously broadened, we speculate that the emission spectrum is as well. If that is the case, the single-atom emission spectrum would be identical to that reported in Ref. [18] for excitation at 786 nm.

Samples are grown and measured at the coldfinger's base temperature of 3 K. Prior work has shown that the substrate temperature during sample growth has a strong effect on its optical properties; low substrate temperatures are important for good optical pumping and readout of spin states [19].

Sample growth begins with neon deposition; the thickness of the neon film during growth is measured by thin-film interference. Rb deposition typically begins after reaching a sample thickness on the order of 1  $\mu m$  and continues for  $\sim\!100$  s. During this time, the sample growth rate is on the order of 4 nm/s. Neon continues to deposit after the Rb flux stops, reaching a typical sample thickness of  $\sim\!\!4~\mu m$ .

Typical sample growth results are shown in Fig. 2. As with all LIF data shown in this paper, this is background-subtracted data. A background image measured prior to sample deposition is subtracted to eliminate a "false fluorescence" signal

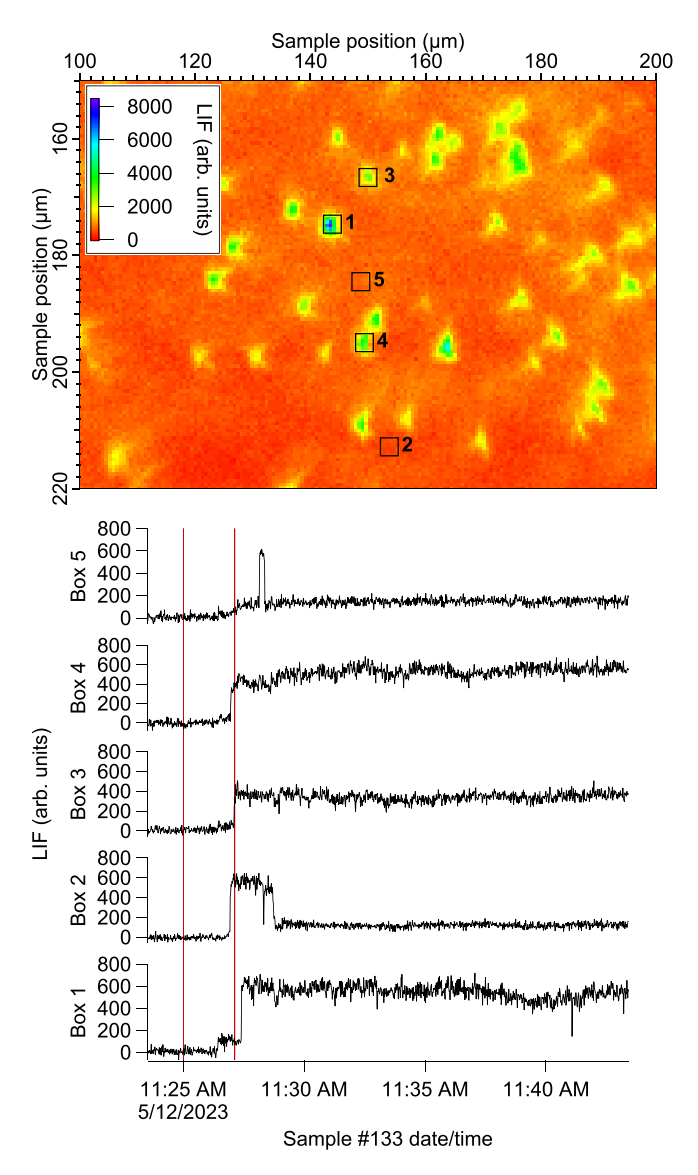


FIG. 2. Top: LIF image of the sample. This image was taken three hours after sample deposition, exciting with linearly polarized light. Bottom: LIF during sample deposition for the five boxes shown in the top image. The red lines indicate when the Rb dispenser used to produce atomic rubidium was turned on and off; the Rb flux lags the current applied to the dispenser.

from the apparatus; the subtracted background is comparable to the LIF signal from the brightest atoms in the sample.

As seen in Fig. 2, the LIF signal from some atoms appears and then abruptly disappears during the deposition process. The mechanism behind this disappearance is not understood. However, the atoms that survive the deposition process can typically produce LIF signals for more than 10<sup>9</sup> photon scattering events and multiple weeks of observation. The mechanism behind this slow loss is also not understood, but similar "bleaching" effects are commonly reported for matrix-isolated atoms [20,21,24,25].

As seen in Fig. 2, the LIF signals from different atoms vary significantly. Unfortunately, it is difficult to characterize the distribution of brightnesses, as very dim atoms would be undetectable. We attribute the variations in brightness primarily to a varying LIF quantum efficiency (QE), the probability

of emitting a photon after excitation. While we do not know for certain the physical mechanism behind the large variations in QE, we suspect it is from variations in trapping sites, which are known to have a large effect on the optical properties of trapped atoms [21,25,26].

To measure the LIF QE of the trapped Rb atoms, we calculate the photon scattering cross section from the homogeneously broadened absorption spectrum of the ensemble [19], under the assumption that the Einstein A coefficient for the Rb transition [27] is unchanged in the matrix. Combining this with the measured laser intensity, we determine the atomic excitation rate. We determine the atomic emission rate from the camera signal integrated over a  $3\times3$  µm region of the sample (using the change in signal that occurs at the appearance of an atom, so as to avoid erroneously including background signal), along with the camera's specified QE averaged over the emission spectrum of the Rb atom [18], and our estimate of the light collection efficiency. By comparing the excitation rate to the emission rate we find a QE of  $\gtrsim$ 0.4 for the brightest atoms we observe. This is a lower limit because a nonnegligible amount of signal lies outside our region of integration. However, the signal to noise of our system makes accurate measurement of the "tails" difficult.

We note that prior work with Rb atoms trapped in neon measured an ensemble LIF QE of 6% [18]. However, the radiative lifetime—as measured via LIF—indicated a QE on the order of 70% [18]. The discrepancy between these two numbers was attributed to a varying LIF QE from atom to atom: the LIF measurements of the radiative lifetime will be dominated by those atoms with a high QE. Our measurements of single atoms are consistent with this interpretation of the ensemble results.

We optically pump the spin states of the atoms by exciting with circularly polarized laser light in the presence of a  $\sim$ 120 G magnetic field which is roughly parallel to the laser beam. The optical pumping should put the atoms into a (semi) dark state, reducing the LIF [19]. We can verify that this is the case—and measure the "contrast" of the spin-state readout—by applying a continuous RF magnetic field to drive population between the  $m_F$  levels and depolarize the spin state.

The applied magnetic field is sufficiently large that the different RF transitions between adjacent  $m_F$  states can be spectroscopically resolved [19]. In the case of <sup>85</sup>Rb, we simultaneously drive all six  $\Delta m=1$  transitions between the seven  $m_F$  states of the F=3 manifold; in the case of <sup>87</sup>Rb, we drive all four transitions between the five  $m_F$  states of the F=2 manifold. Typical results are shown in Fig. 3.

We define the contrast as the difference in the LIF between RF on and off, divided by the LIF with RF on. With this definition, gas phase atoms can achieve a contrast approaching a value of one, as optical pumping with the RF off would produce a nearly perfect dark state.

For each sample, we hand select five to nine of the brightest atoms, well isolated from their neighbors, and measure their contrast. For 69 atoms over ten samples, the highest single-atom contrast levels observed were 0.25 for <sup>85</sup>Rb and 0.31 for <sup>87</sup>Rb. The average contrast observed for <sup>85</sup>Rb is 0.15, with a standard deviation of 0.05; the average for <sup>87</sup>Rb is 0.20 with a standard deviation of 0.06. A histogram of all measurements is shown in Fig. 4.

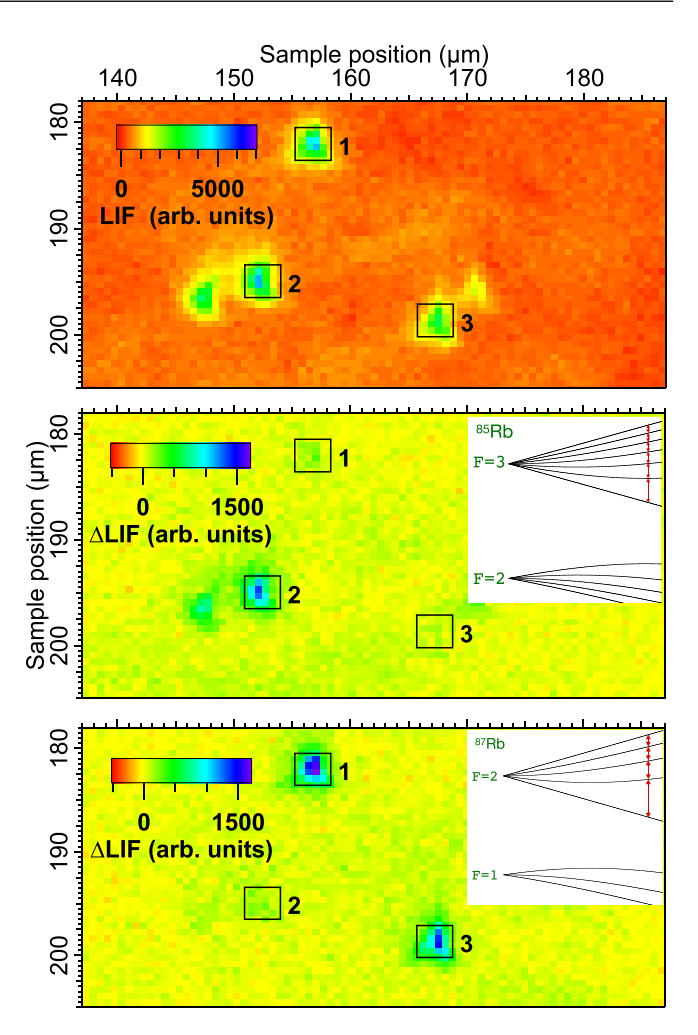


FIG. 3. The upper figure shows the background-subtracted LIF from a sample excited with circularly polarized light. The middle and bottom figures show the change in LIF when applying RF drive on resonance with the <sup>85</sup>Rb and <sup>87</sup>Rb Zeeman transitions, respectively. From this, we conclude the region labeled "2" contains a <sup>85</sup>Rb atom, while regions 1 and 3 contain <sup>87</sup>Rb.

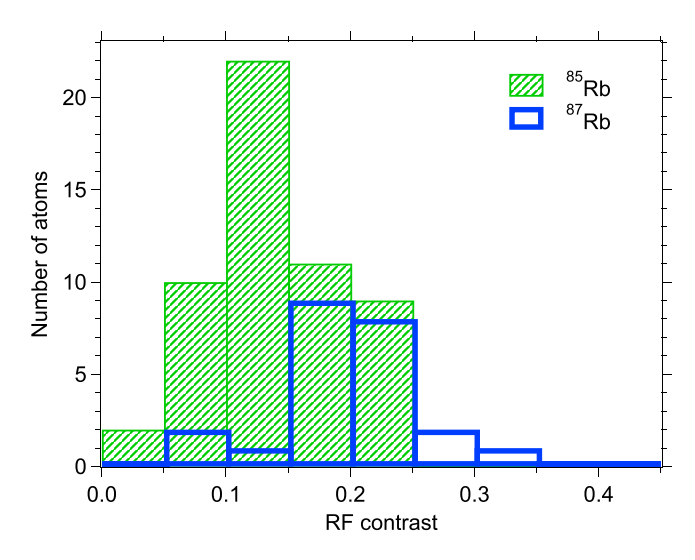


FIG. 4. Histogram of the spin-readout contrast of individual atoms, as described in the text.

We note that the contrast is limited by a combination of imperfect optical pumping, imperfect optical readout, imperfect depolarization from the RF drive, and stray LIF signal from other isotopes in the region analyzed as well as apparatus-scattered light. We suspect the first two are the dominant sources of the reduced contrast. We believe the slightly superior performance of  $^{87}$ Rb is due to its smaller nuclear spin I, giving rise to a smaller number of  $m_F$  levels.

Comparing the single-atom LIF contrast to prior ensemble measurements using circular dichroism, the average single-atom contrast is comparable to the best results reported for ensemble measurements [19]. The best single atoms are superior to the best ensemble measurements, as would be expected for a system with nonuniform contrast.

The readout contrast observed here is only slightly lower than results reported for NV ensembles [28], near-surface NV's [29–31], and molecular qubits [32]. However, the contrast is significantly smaller than the best results reported for single NV's in the bulk [33]. We note that in the protocol we have previously employed for magnetic sensing, the state readout is done when the atom is in one of its two stretch spin states [19], which should provide roughly twice the contrast of the measurements performed here.

The ensemble spin coherence time  $T_2$  was previously reported in Ref. [19]. With appropriate dynamical decoupling sequences (compatible with protocols to sense nuclear spins), a  $T_2$  on the order of 0.1 s was measured. It was noted that  $T_2$  was limited by magnetic field noise from fluctuating <sup>21</sup>Ne spins in the solid, and a range of  $T_2$ 's were present for a given sample. As such, we would expect different single rubidium atoms to have different values of  $T_2$ , with a typical value comparable to that reported in Ref. [19]. An ensemble longitudinal spin relaxation time  $T_1$  on the order of 1 s was reported in Ref. [19]. As this is significantly longer than  $T_2$ —the relevant parameter for quantum sensing—it is not an important limitation on  $T_2$ , and we have not investigated it further.

The ensemble spin dephasing time  $T_2^*$  was also reported in Ref. [19]. Superposition states corresponding to Larmor precession states exhibited  $T_2^*$  values on the order of 10  $\mu$ s, which was limited by inhomogenous broadening in the solid. As such, we would expect to obtain much longer values of  $T_2^*$  for a single atom; unfortunately, this was not the case due to technical issues. We perform optically detected magnetic resonance (ODMR) spectroscopy by monitoring the fluorescence as we drive a single Zeeman transition; the linewidth of the transition is inversely proportional to  $T_2^*$ . As seen in Fig. 5, as the amplitude of the drive is reduced, the linewidth narrows, but the signal disappears before we observes linewidths as narrow as those measured with an ensemble: 70 kHz for the  $^{85}$ Rb transition shown here [19]. We attribute this to the known magnetic field drift in our laboratory.

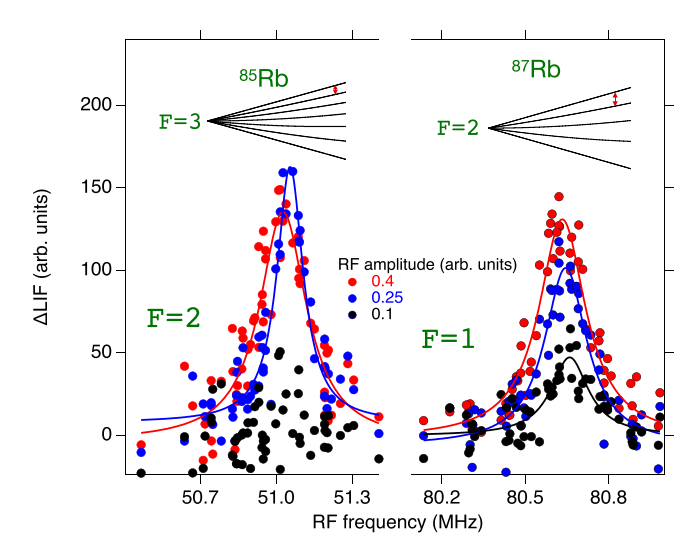


FIG. 5. The change in the LIF signal due to an applied RF magnetic field, shown as a function of the RF frequency for three different magnetic field amplitudes. Data from two different atoms in the same sample are shown. For the <sup>85</sup>Rb atom (on the left), the signal from driving the  $m_F = +2 \leftrightarrow +3$  transition in the F=3 manifold is shown; the Lorentzian fits give linewidths of 225 and 126 kHz FWHM. For <sup>87</sup>Rb (on the right) the  $m_F = +1 \leftrightarrow +2$  transition is shown; the fit linewidths are 205, 185, and 163 kHz FWHM.

In future work, we hope to characterize the readout fidelity of the spin state. We note that techniques have been developed for NV centers which provide high readout fidelity even in the presence of poor optical contrast [30,34]. However, in the absence of such a scheme, the contrast levels reported here—combined with the depopulation pumping properties of the spin state previously reported [19]—would make achieving high readout fidelity impossible. This would preclude using these atoms for quantum computing applications [35]. However, we expect it to be sufficient for quantum sensing applications, where an imperfect readout fidelity can be overcome with modest amounts of averaging [1]. In future work, we hope to use the system for single-atom NMR measurements by the same techniques we previously used for ensemble NMR spectroscopy [19], and ultimately for the imaging of single nuclear spins, by techniques similar to those demonstrated with NV's [8].

This material is based upon work supported by the National Science Foundation under Grants No. PHY-1912425 and No. PHY-2309280. We gratefully acknowledge contributions to the construction of the experimental apparatus from Wade J. Cline and Carl D. Davison, Jr.; contributions to the data aquisition system from Eegan Ram; experimental contributions from Hamed Goli Yousefabad; and helpful conversations with David Patterson.

<sup>[1]</sup> C. L. Degen, F. Reinhard, and P. Cappellaro, Quantum sensing, Rev. Mod. Phys. **89**, 035002 (2017).

<sup>[2]</sup> J. R. Maze, P. L. Stanwix, J. S. Hodges, S. Hong, J. M. Taylor, P. Cappellaro, L. Jiang, M. V. Gurudev Dutt, E. Togan, A. S. Zibrov, A. Yacoby, R. L. Walsworth, and M. D. Lukin, Nanoscale magnetic sensing with an individual electronic spin in diamond, Nature (London) 455, 644 (2008).

<sup>[3]</sup> C. L. Degen, Scanning magnetic field microscope with a diamond single-spin sensor, Appl. Phys. Lett. **92**, 243111 (2008)

<sup>[4]</sup> A. Ajoy, U. Bissbort, M. D. Lukin, R. L. Walsworth, and P. Cappellaro, Atomic-scale nuclear spin imaging using quantum-assisted sensors in diamond, Phys. Rev. X 5, 011001 (2015).

- [5] S. Kolkowitz, Q. P. Unterreithmeier, S. D. Bennett, and M. D. Lukin, Sensing distant nuclear spins with a single electron spin, Phys. Rev. Lett. 109, 137601 (2012).
- [6] T. H. Taminiau, J. J. T. Wagenaar, T. van der Sar, F. Jelezko, V. V. Dobrovitski, and R. Hanson, Detection and control of individual nuclear spins using a weakly coupled electron spin, Phys. Rev. Lett. 109, 137602 (2012).
- [7] N. Zhao, J. Honert, B. Schmid, M. Klas, J. Isoya, M. Markham, D. Twitchen, F. Jelezko, R.-B. Liu, H. Fedder, and J. Wrachtrup, Sensing single remote nuclear spins, Nat. Nanotechnol. 7, 657 (2012).
- [8] M. H. Abobeih, J. Randall, C. E. Bradley, H. P. Bartling, M. A. Bakker, M. J. Degen, M. Markham, D. J. Twitchen, and T. H. Taminiau, Atomic-scale imaging of a 27-nuclear-spin cluster using a quantum sensor, Nature (London) 576, 411 (2019).
- [9] I. Lovchinsky, A. Sushkov, E. Urbach, N. P. de Leon, S. Choi, K. De Greve, R. Evans, R. Gertner, E. Bersin, C. Müller et al., Nuclear magnetic resonance detection and spectroscopy of single proteins using quantum logic, Science 351, 836 (2016).
- [10] V. S. Perunicic, C. D. Hill, L. T. Hall, and L. C. L. Hollenberg, A quantum spin-probe molecular microscope, Nat. Commun. 7, 12667 (2016)
- [11] B. L. Dwyer, L. V. H. Rodgers, E. K. Urbach, D. Bluvstein, S. Sangtawesin, H. Zhou, Y. Nassab, M. Fitzpatrick, Z. Yuan, K. De Greve, E. L. Peterson, H. Knowles, T. Sumarac, J.-P. Chou, A. Gali, V. V. Dobrovitski, M. D. Lukin, and N. P. de Leon, Probing spin dynamics on diamond surfaces using a single quantum sensor, PRX Quantum 3, 040328 (2022).
- [12] E. Janitz, K. Herb, L. A. Völker, W. S. Huxter, C. L. Degen, and J. M. Abendroth, Diamond surface engineering for molecular sensing with nitrogenvacancy centers, J. Mater. Chem. C 10, 13533 (2022).
- [13] Z. Yuan, L. V. H. Rodgers, J. Rovny, S. Sangtawesin, S. Srinivasan, J. Allred, N. P. de Leon, and P. Gumann, Ultrahigh vacuum surface chemistry for nanoscale sensors in diamond, in *Quantum 2.0 Conference and Exhibition*, Technical Digest Series (Optica Publishing Group, Boston, MA, 2022), paper QTu2A.11.
- [14] S. Upadhyay, U. Dargyte, D. Patterson, and J. D. Weinstein, Ultralong spin-coherence times for rubidium atoms in solid parahydrogen via dynamical decoupling, Phys. Rev. Lett. 125, 043601 (2020).
- [15] A. Kaczor, I. D. Reva, L. M. Proniewicz, and R. Fausto, Matrix-Isolated monomeric tryptophan: Electrostatic interactions as nontrivial factors stabilizing conformers, J. Phys. Chem. A 111, 2957 (2007).
- [16] A. Kaczor, I. D. Reva, L. M. Proniewicz, and R. Fausto, Importance of entropy in the conformational equilibrium of phenylalanine: A matrix-isolation infrared spectroscopy and density functional theory study, J. Phys. Chem. A 110, 2360 (2006).
- [17] S. G. Stepanian, I. D. Reva, E. D. Radchenko, and L. Adamowicz, Conformational behavior of  $\alpha$ -alanine. matrixisolation infrared and theoretical DFT and ab initio study, J. Phys. Chem. A **102**, 4623 (1998).
- [18] D. M. Lancaster, U. Dargyte, S. Upadhyay, and J. D. Weinstein, Radiative properties of rubidium atoms trapped in solid neon and parahydrogen, Phys. Rev. A 103, 052614 (2021).

- [19] U. Dargyte, D. M. Lancaster, and J. D. Weinstein, Optical and spin-coherence properties of rubidium atoms trapped in solid neon, Phys. Rev. A **104**, 032611 (2021).
- [20] C. Chambers, T. Walton, D. Fairbank, A. Craycraft, D. Yahne, J. Todd, A. Iverson, W. Fairbank, A. Alamre, J. Albert *et al.* (nEXO Collaboration), Imaging individual barium atoms in solid xenon for barium tagging in nEXO, Nature (London) 569, 203 (2019).
- [21] A. N. Kanagin, S. K. Regmi, P. Pathak, and J. D. Weinstein, Optical pumping of rubidium atoms frozen in solid argon, Phys. Rev. A 88, 063404 (2013).
- [22] S. M. Mansfield and G. Kino, Solid immersion microscope, Appl. Phys. Lett. 57, 2615 (1990).
- [23] W. S. Bakr, J. I. Gillen, A. Peng, S. Fölling, and M. Greiner, A quantum gas microscope for detecting single atoms in a Hubbard-regime optical lattice, Nature (London) 462, 74 (2009)
- [24] I. Gerhardt, K. Sin, and T. Momose, Excitation and emission spectra of rubidium in rare-gas thin-films, J. Chem. Phys. **137**, 014507 (2012).
- [25] S. Upadhyay, U. Dargyte, V. D. Dergachev, R. P. Prater, S. A. Varganov, T. V. Tscherbul, D. Patterson, and J. D. Weinstein, Spin coherence and optical properties of alkali-metal atoms in solid parahydrogen, Phys. Rev. A 100, 063419 (2019).
- [26] S. L. Kupferman and F. M. Pipkin, Properties of rubidium atoms trapped in a solid argon matrix, Phys. Rev. 166, 207 (1968).
- [27] J. E. Sansonetti, W. C. Martin, and S. L. Young, *Handbook of Basic Atomic Spectroscopic Data (version 1.1.3)* (NIST, 2013) http://physics.nist.gov/PhysRefData/Handbook/.
- [28] J. F. Barry, J. M. Schloss, E. Bauch, M. J. Turner, C. A. Hart, L. M. Pham, and R. L. Walsworth, Sensitivity optimization for NV-diamond magnetometry, Rev. Mod. Phys. 92, 015004 (2020).
- [29] Z. Yuan, M. Fitzpatrick, L. V. H. Rodgers, S. Sangtawesin, S. Srinivasan, and N. P. de Leon, Charge state dynamics and optically detected electron spin resonance contrast of shallow nitrogen-vacancy centers in diamond, Phys. Rev. Res. 2, 033263 (2020).
- [30] J.-C. Jaskula, B. J. Shields, E. Bauch, M. D. Lukin, A. S. Trifonov, and R. L. Walsworth, Improved quantum sensing with a single solid-state spin via spin-to-charge conversion, Phys. Rev. Appl. 11, 064003 (2019).
- [31] J. Taylor, P. Cappellaro, L. Childress, L. Jiang, D. Budker, P. Hemmer, A. Yacoby, R. Walsworth, and M. Lukin, Highsensitivity diamond magnetometer with nanoscale resolution, Nat. Phys. 4, 810 (2008).
- [32] S. L. Bayliss, P. Deb, D. W. Laorenza, M. Onizhuk, G. Galli, D. E. Freedman, and D. D. Awschalom, Enhancing spin coherence in optically addressable molecular qubits through host-matrix control, Phys. Rev. X 12, 031028 (2022).
- [33] L. Robledo, L. Childress, H. Bernien, B. Hensen, P. F. Alkemade, and R. Hanson, High-fidelity projective read-out of a solid-state spin quantum register, Nature (London) 477, 574 (2011).
- [34] B. J. Shields, Q. P. Unterreithmeier, N. P. de Leon, H. Park, and M. D. Lukin, Efficient readout of a single spin state in diamond via spin-to-charge conversion, Phys. Rev. Lett. 114, 136402 (2015).
- [35] J. M. Martinis, Qubit metrology for building a fault-tolerant quantum computer, npj Quantum Inf. 1, 15005 (2015).